

Significant mutual inclinations between the stellar spin and the orbits of both planets in the HAT-P-11 system

QIER AN ¹ TIGER LU ² G. MIREK BRANDT ¹ TIMOTHY D. BRANDT ^{3,1} AND GONGJIE LI ⁴

¹*Department of Physics, University of California, Santa Barbara, Santa Barbara, CA 93106, USA*

²*Department of Astronomy, Yale University, 52 Hillhouse, New Haven, CT 06511, USA*

³*Space Telescope Science Institute, 3700 San Martin Dr., Baltimore, MD 21218, USA*

⁴*Center for Relativistic Astrophysics, School of Physics, Georgia Institute of Technology, Atlanta GA 30332, USA*

Submitted to AJ

ABSTRACT

Planet-star and planet-planet obliquity encode a planetary system’s dynamical history, but both obliquities are hard to measure for misaligned systems with close-in companions. HAT-P-11 is a K4 star with two known planets: a close-in, misaligned super-Neptune with a ≈ 5 -day orbit, and an outer super-Jupiter with a ≈ 10 -year orbit. In this work we present a joint orbit fit of HAT-P-11 system with astrometry and RV data. By combining our results with previous constraints on the orientation of the star and the inner planet, we find that all three angular momenta—those of the star, planet b, and planet c—are significantly misaligned. We confirm the status of planet c as a super-Jupiter, with $3.06 \pm 0.42 M_{\text{Jup}}$ at a semimajor axis of 4.192 ± 0.07 AU, and planet b’s mass of $M_b \sin i_b = 0.073 \pm 0.0053 M_{\text{Jup}}$. We present the posterior probability distribution of obliquity between star A and planet c, and between planet b and planet c.

Keywords: —

1. INTRODUCTION

The main reservoirs of angular momentum in the Solar system—the Sun’s spin and the planetary orbits—are all closely aligned (Souami & Souchay 2012). This observational fact has informed theories of the Solar system planets’ formation in a stable protoplanetary disk (see a review in Nesvorný 2018). Exoplanetary systems show a much wider range of planet masses and orbital separations than our own Solar system, from hot Jupiters and mini-Neptunes to packed planetary systems within the orbit of Venus (Gillon et al. 2017). The masses and orbits of these planets may be measured with transits and radial velocities, but stellar obliquities—the angles between the stellar spin and planet orbit—are harder to measure. We do not know the extent to which a diversity in exoplanetary masses, eccentricities, and periods is matched by a diversity in obliquities.

Tidal forces tend to damp obliquity between planets and their host star, and can efficiently align close-in planets (Dawson 2014). Stellar-disk obliquity also tends to damp, which could lead to low obliquities for planets formed in that disk (Valsecchi & Rasio 2014; Li & Winn 2016). Despite this, moderate degrees of stellar-

disk misalignment may be excited, notably in the presence of a binary companion (Zanazzi & Lai 2018). A planet that forms in a disk will inherit the angular momentum of its parent disk. Larger stellar obliquities may be produced either by more violent events like planet-planet scattering (Chatterjee et al. 2008; Nagasawa & Ida 2011), or by ZLK cycles (von Zeipel 1910; Lidov 1962; Kozai 1962).

Projected obliquities have been measured for a modest number of exoplanetary systems, mostly through the Rossiter-McLaughlin effect (Rossiter 1924; McLaughlin 1924). As a planet transits different parts of a star spinning edge-on, redshifted and blueshifted patches of the stellar surface can be sequentially occulted, leading to slight variations in absorption line profiles. The Rossiter-McLaughlin effect is only measurable for transiting planets; obliquities of more widely separated planets that are unlikely to transit are much harder to measure. Misalignment between the orbits of different planets (planet-planet obliquity) in an exoplanetary system may sometimes be constrained by transit timing variations (Holman & Murray 2005; Agol et al. 2005), especially when multiple planets transit (Kane & Torres

2017; Agol et al. 2021). Multiple transiting planets are likeliest in an aligned system (Morton & Winn 2014), and transit timing variations are most effective at measuring systems with low planet-planet obliquity.

Planet-star and planet-planet obliquity encode the dynamical history of a system: they show the final result of dynamical excitation, scattering, and tidal damping. This full set of obliquity measurements is very difficult to obtain for an individual system. Transit timing variations are most easily measured for closely packed systems in which multiple planets transit. Multiple transiting planets are likeliest when their orbits are aligned, and dynamically packed systems typically cannot be stable with significant obliquity (Albrecht et al. 2013). Planet-planet obliquities are very difficult to measure for misaligned systems, while planet-star obliquities may not be measurable for widely-separated planets. We lack a full set of obliquity constraints for a dynamically hot system.

The HAT-P-11 system consists of a super-Neptune planet on a ≈ 5 -day orbit (Bakos et al. 2010) and an outer, super-Jupiter on a ≈ 10 -year orbit (Yee et al. 2018). The inner planet (planet b) has a large projected obliquity with the stellar spin (Sanchis-Ojeda & Winn 2011). The outer planet (planet c) has been posited to have a significant inclination relative to the inner planet in order to explain this obliquity (Yee et al. 2018). Those authors had no direct observational support for their hypothesis, but did suggest that future data from the Gaia satellite (Gaia Collaboration et al. 2016) could offer such evidence.

In this paper we combine RVs, absolute astrometry from Hipparcos and Gaia, and projected obliquity constraints from Sanchis-Ojeda & Winn (2011) to constrain the alignment of all three main angular momentum vectors in the HAT-P-11 system. These include the first measurements of the relative inclinations between the outer planet (planet c) and the star, and between planet c and planet b. We confirm that there does indeed exist a significant misalignment between the orbits of planet c and b.

We organize the paper as follows. In Section 2, we summarize the data collected and adopted for this study. We discuss details of orbit fitting and obliquity calculation in Section 3. The orbital solution and obliquity calculation results are presented in Section 4. We discuss the results and conclude in Section 5. We investigate the dynamical origin of this misalignment in a follow-up paper (Lu et. al in prep, hereafter Paper 2).

We combine four types of archival data for our analysis of the HAT-P-11 system: radial velocities (RVs) and absolute astrometry of the host star, a measurement of the projected obliquity between the host star and the inner planet, planet b, and the edge-on inclination of planet b’s orbit from its transits. In this section we summarize each of these sources of data in turn. Our orbital fit relies on RVs and absolute astrometry, while the projected obliquity constrains the relative orientation of the three main angular momentum vectors in the system.

We adopt RVs from the High-Resolution Échelle Spectrometer (HIRES, Vogt et al. 1994) on the Keck telescope; the RVs were tabulated by Yee et al. (2018). Many of these RVs were taken as part of the long-running California Planet Search (CPS, Howard et al. 2010). Spectra were taken with the iodine cell in place for wavelength calibration and reduced using the CPS pipeline. The data set consists of 253 individual RV measurements from 134 unique nights covering a ≈ 10 year baseline, from late 2007 to late 2017 with a median precision of 1.3 m s^{-1} . We use the same subset of RV data as Yee et al. (2018), i.e., we keep all points flagged as 1 in their Table 1. This leaves 144 of the initial 253 RVs. These RVs were used by Yee et al. (2018) to discover an outer planet, planet c, and to fit for the orbits of both planet b and planet c.

We adopt absolute astrometry of the star HAT-P-11 (=HIP 97657) from the Hipparcos-Gaia Catalog of Accelerations (HGCA, Brandt 2018, 2021). The HGCA cross-calibrates Hipparcos and Gaia astrometry onto a common reference frame and ensures that the errors are statistically well-behaved. There are three measured proper motions in the HGCA: one from Hipparcos, one from Gaia, and a long-term proper motion from the position shift between Hipparcos and Gaia. Differences between the three proper motions in the HGCA indicate acceleration in an inertial reference frame. HAT-P-11 itself has a χ^2 value of 42.5 for a model of constant proper motion, i.e., the long-term proper motion differs from the Gaia proper motion at more than 6σ significance.

While HAT-P-11 is accelerating between Hipparcos and Gaia, in both missions it is satisfactorily fit by a sky path assuming constant proper motion. In the original Hipparcos reduction (ESA 1997) HAT-P-11 has an F2 value just over 2, indicating a fit $\approx 2\sigma$ worse than expected with a constant proper motion sky path. In the Hipparcos re-reduction van Leeuwen (2007) a constant proper motion sky path fits HAT-P-11’s astrometry slightly better than for the average star. In Gaia EDR3 (Lindgren et al. 2020), the star has a renormal-

2. DATA

ized unit weight error (RUWE) of 0.94, slightly better than a value of 1 that is typical for a single star.¹

A satisfactory fit to single star motion in both Hipparcos and Gaia EDR3 indicates an orbital period significantly longer than the ≈ 3 -year baseline of these missions. Planet c, with its ≈ 10 -year orbit (Yee et al. 2018), naturally accounts for the discrepancy between the long-term and Gaia proper motions while also explaining the good fits to single star motion within both Hipparcos and Gaia. In the following section, we fit orbits to the HAT-P-11 system under the hypothesis that planet c is almost entirely responsible for the observed astrometric acceleration.

Our final input measurement for the HAT-P-11 system is the projected obliquity derived by Sanchis-Ojeda & Winn (2011). This measurement is from a combination of radial velocities via the Rossier-McLaughlin effect and modeling of starspots as the planet crosses the active stellar surface. Sanchis-Ojeda & Winn (2011) find a bimodal probability distribution of obliquities, of 106_{-11}^{+15} degrees (edge-on solution) and 97_{-4}^{+8} degrees (pole-on solution). The measurement of the obliquity between the star and planet b does not directly constrain our orbital fit, but it does constrain the relative orientation of the three dominant angular momenta in the system: the spin of the star and the orbits of planets b and c.

3. METHODOLOGY

3.1. Orbit fit

We fit Keplerian orbital elements to radial velocities and absolute astrometry using the code *orvara* Brandt et al. (2021d). *orvara* uses parallel-tempered Markov chain Monte Carlo (MCMC) with *pemcee* (Foreman-Mackey et al. 2013; Vousden et al. 2016). We use a parallel-tempered MCMC with 20 temperatures; for each temperature we use 100 walkers with 400,000 steps per walker, and each walker is thinned by a factor of 400. We use the coldest chain for statistical inference. Our MCMC chains converged after 100,000 steps; we conservatively discard the first 200,000 as burn in. We use the standard *orvara* priors for most parameters, as in e.g., Brandt et al. (2021d); Li et al. (2021); Brandt et al. (2021a). These standard priors include a geometric prior on inclination ($p(i) = \sin i$), log-uniform prior in semimajor axis, and uniform priors on eccentricity, orbital phase, argument of periastron, and orientation in the plane of the sky. We adopt an informative prior of 0.81 ± 0.03 for the host star’s mass (Dai et al. 2018)

and uniform priors on the masses of the two planets (b & c): uniform between 0 and $100M_{\text{Jup}}$. These differ from the log-uniform companion mass priors that *orvara* uses by default. A summary of priors is indicated in Table 1.

At each MCMC step, absolute astrometry is processed by *htof* (Brandt et al. 2021b; Brandt & Michalik 2020). Given a set of orbital parameters, *htof* models the absolute astrometry that Gaia and Hipparcos would observe. Using the epoch absolute astrometry itself is not yet possible for Gaia, while these epoch astrometry in Hipparcos are problematic for orbit fitting (Brandt et al. 2023). Instead, *htof* uses the epochs and orientations of observations from the Gaia GOST service², and both *Hipparcos* and *Hipparcos 2* (from the 2014 Java Tool IAD but released in 2022) from the European Space Agency archive³ to compute synthetic epoch astrometry. From these, we obtain synthetic positions and proper motions that can be statistically compared to the HGCA values.

As is standard, we use synthetic absolute astrometry from the Gaia GOST service⁴, and both *Hipparcos* 1997 IAD and *Hipparcos* 2007 (from the 2014 Java Tool IAD but released in 2022) come from the European Space Agency archive⁵.

Orvara simultaneously fits HGCA absolute astrometry and the HIRES RVs described in the previous section. We use the same subset of RV data as those authors (i.e., keeping all points flagged as 1 in their Table 1). This leaves 144 of the initial 253 RVs. However, our orbit-fitting results are almost identical even if we include all 253 RV points. The only noticeable difference is that the inferred secondary mass in this no-reject case is $1\sigma \approx 0.4M_{\text{Jup}}$ smaller. The RV fit includes an analytic marginalization of the unknown RV zero point, i.e., the RV of the system barycenter.

Our *orvara* fits to the absolute astrometry and RVs can constrain many, though not all, of the orbital parameters. The inclination of the inner planet (planet b) is almost entirely unconstrained by *orvara*: the motion induced by planet b’s orbit on the star, the sub-microarcsecond semi-amplitude signal, is too small to be detectable in either Hipparcos or Gaia. Besides, given planet b’s short orbit of ≈ 5 days and *Hipparcos* and *Gaia* long baselines of over years, time-averaged astrometric signal are undetectable for planet b. This inclination is instead constrained to be nearly edge-on by

² <https://gaia.esac.esa.int/gost/>

³ <https://www.cosmos.esa.int/web/hipparcos/interactive-data-access>

⁴ <https://gaia.esac.esa.int/gost/>

⁵ <https://www.cosmos.esa.int/web/hipparcos/interactive-data-access>

¹ Gaia EDR3 astrometry is identical to Gaia DR3 astrometry for single star fits.

the light curves of the planetary transits (Bakos et al. 2010). The position angle of planet b’s orbit—its orientation in the plane of the sky—is unconstrained by any observations. All of the orbital parameters for planet c can be meaningfully constrained in our fit. Table 1 describes MCMC priors and posterior orbital parameters of planet b and planet c, where the posterior mass distribution for planet b is reported in the form of $M_b \sin i_b$, the lower mass limit, though transit data confirm that $\sin i \approx 1$.

3.2. Obliquity calculation

We use the orbital posterior of HAT-P-11 c from our orbit fit to directly calculate the planet’s three-dimensional orbital angular momentum vector (note that there turn out to be two possible inclination modes). Sanchis-Ojeda & Winn (2011) solved for the posterior of the 3D stellar spin axis, albeit up to one unknown angle, λ . This is the angle that the spin vector is rotated about the line-of-sight vector to Earth⁶. Sanchis-Ojeda & Winn (2011) measured this, in short, by combining Rossiter-McLaughlin (RM) measurements of the obliquity between A and b (see, Hirano et al. 2011; Winn et al. 2010) with Kepler light-curve variability and models of stellar active latitudes and starspot locations.

To solve for the obliquity between the star A and planet c (hereafter ψ_{Ac}), we adopt the marginalized stellar inclination i_{star} posteriors from Table 3 of Sanchis-Ojeda & Winn (2011). The pole-on case is $i_{\text{star}} = 168^\circ \pm_5^+$ and edge-on is $i_{\text{star}} = 80^\circ \pm_3^+$. According to Sanchis-Ojeda & Winn (2011), their two predictions of $v \sin i_{\text{star}} = (2\pi R_*/R_{\text{rot}}) \sin i_{\text{star}}$ value equal 0.5 km/s (pole-on) and 1.3 km/s (edge-on), which each agree with the observed value of 1.5 ± 1.5 km/s from Bakos et al. (2010). However, modern measurements of $v \sin i_{\text{star}}$, 2 ± 0.5 km/s from Brewer & Fischer (2018) and 3.2 ± 1 km/s from Petigura et al. (2017), slightly favor (by about 2σ to 3σ) the edge-on scenario. We include and analyze the edge-on and pole-on stellar-spin cases separately.

We have a full 3d stellar spin vector given a stellar inclination i_{star} and a sky-plane angle λ which separates the spin and orbital angular momenta vectors. We already have the planet’s three-dimensional orbital angular momentum, but λ is unknown and can assume any value between 0 and 2π . Thus to find the obliquity between A and c, we calculate the dot product between the two vectors and marginalize over the uniform dis-

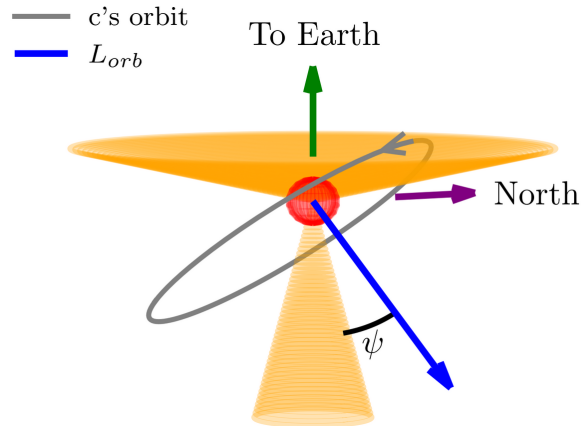


Figure 1. Orbital architecture of the HAT-P-11 system. The star (not to scale) is represented by the red sphere. North and line-of-sight (to Earth) are given. The orbit of c is described in grey, while the inner planet b is not shown. The two orange cones represent the possible stellar spins that Sanchis-Ojeda & Winn (2011) derived from obliquity measurements of b. The upper cone is the set of edge-on stellar-spin configurations and the bottom cone give the pole-on solutions. The blue vector is the orbital angular momentum of the outer planet c.

tribution of sky-plane angles λ . The dot product (and thus $\cos \psi_{Ac}$) may be calculated with Equation (8) of Sanchis-Ojeda & Winn (2011):

$$\cos \psi = \cos i_{\text{star}} \cos i_{\text{orbit}} + \sin i_{\text{star}} \cos \lambda \sin i_{\text{orbit}}.$$

It depends on only the stellar and orbital inclinations (i_{star} and i_c) and λ .

The orbital architecture is plotted in Figure 1, where the orange cones are sets of possible stellar spins (upper cone for edge-on and bottom cone for pole-on), and the blue vector shows planet c’s orbital angular momentum. The cosine of the obliquity between planet c and the star A is the dot product of L_{orb} with all vectors living on the two spin cones. One obliquity possible is indicated by ψ , which is roughly 20 degrees.

We solve for the obliquity between b and c in an identical fashion, only with i_b taking the place of i_{star} , and i_b being constrained by the planet’s transit light curves. Since we do not have a full 3d normal vector of planet b’s orbit, we have no constrain on the sky-plane angle λ . Therefore, in ψ_{bc} calculation, we assume λ can be any value between 0 to 2π . Including *Hipparcos-Gaia* accelerations in the 3-body fit breaks the $m \sin i$ degeneracy of the long-period outer planet, but the accelerations do not constrain the inclination i_b of the inner planet due to that planet’s tiny mass and short period, and its resulting sub- μas astrometric orbital amplitude. We use $i_b = 88^\circ.5 \pm 0^\circ.6$ from Stassun et al. (2017), who measured it from the transiting planet’s impact parameter,

⁶ λ is also commonly referred to as the projected obliquity, when it is in reference not to the line-of-sight vector but the orbital angular momentum vector of a specific planet.

and draw values of λ from a uniform distribution from 0 to 2π .

4. RESULTS

Here we present the results of a 3-body orbit fit of the HAT-P-11 system, as well as the obliquity measurements between the primary star HAT-P-11 A and its outer planet c, and the obliquity between inner planet b and outer planet c. A summary of the prior and best-fit posterior orbital parameters of the HAT-P-11 system is reported in Table 1. The top panel of Figure 2 presents relative orbits of the outer planet c drawn from the MCMC posterior samples, together with the best-fit orbit in black. The bottom panel of Figure 2 shows the observed RVs of the primary star together with random orbits drawn from the MCMC posterior and the best fit orbit in black. We present the corner plot of posterior orbital elements in Figure 3 for planet b and Figure 4 for planet c. Figures 5-7 report the probability distribution of obliquity between star A and planet c, and between planet b and planet c.

4.1. Orbital Elements of the Planets

RVs constrain the orbital period, eccentricity, and $M \sin i$ of the inner planet, planet b. Our mass, eccentricity, and period agree with those originally determined from transits (Bakos et al. 2010). The inner planet is responsible for the high-frequency RV signal visible in Figure 2. The longer-term variations are due to planet c, whose orbital results we now briefly discuss.

The parameters of planet c are constrained jointly by absolute astrometry and RV data. The presence of an outer planet c is inferred from astrometric acceleration of HAT-P-11 A and the long-term undulation of the RV curve presented in the lower panel of Figure 2; the planet was first identified and fit by Yee et al. (2018) using only RVs. We measure a mass of $3.06 \pm 0.42 M_{\text{Jup}}$ for planet c, confirming its status as a super-Jupiter. Our result of M_c is $\approx 1\sigma$ heavier than the previous value of $2.3_{-0.5}^{+0.7} M_{\text{Jup}}$ from Xuan & Wyatt (2020). That analysis used a previous, less-precise version of Hipparcos-Gaia astrometry based on Gaia DR2 (Brandt 2018). Our semi-major axis of 4.19 ± 0.07 AU agrees with Yee et al. (2018)’s finding of $4.13_{-0.16}^{+0.29}$ AU. Our result also characterizes the orbit with argument of periastron ($\omega = 139^\circ.9 \pm 4^\circ.1$) and eccentricity ($e = 0.560 \pm 0.036$). Our inclination posterior is bimodal, where the peaks of the distribution are close to 30° and 150° .

The upper panel of Figure 2 shows the orbit of planet c in the plane of the sky. The maximum-likelihood orbit is colored black, while the colored lines are randomly chosen from the orbit fitting posteriors.

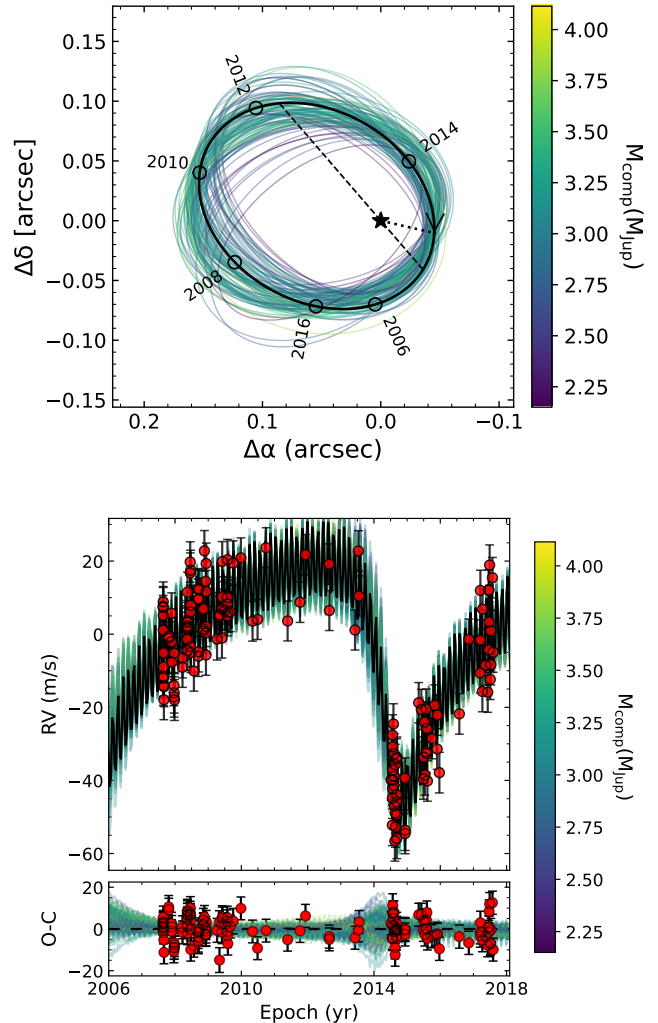


Figure 2. Top: Relative orbits of planet c (in arc seconds) from fitting RVs and absolute astrometry from the v.EDR3 HGCA. One hundred random orbital draws are shown and color-coded by companion mass. Positions at a few selected epochs are displayed for the maximum-likelihood orbital solution (black). The host-star is marked by the star symbol at the origin. **Bottom:** The observed RVs of HAT-P-11 overplotted with the best fit orbit (in black) and a random sampling of other orbits from the MCMC chain. The RV signal includes both the high-frequency oscillations from b and the long-term high-eccentricity undulation of c. The RV residuals with respect to the best fit orbit are in the attached bottom subpanel.

We present the corner plot of planet c’s posterior orbital elements in Figure 4. The smooth, nearly Gaussian contours indicate a well-converged posterior. Most plotted parameters are well constrained except for inclination, in which two modes are reflected with respect to 90° . The degeneracy of inclination can be visualized in the bottom row of plots and in the lower-right 1D histogram. This behavior is common when Hippar-

Table 1. MCMC prior and posterior orbital parameters for HAT-P-11 b and HAT-P-11 c.

Parameter	Prior	Posterior b $\pm 1\sigma$	Posterior c $\pm 1\sigma$
Jit (m/s)	$1/\sigma_{\text{Jit}}$	$5.43^{+0.37}_{-0.34}$	$5.43^{+0.37}_{-0.34}$
M_{pri} (M_{\odot})	$N(0.81, 0.03)$	0.811 ± 0.03	0.811 ± 0.03
M_{sec} (M_{Jup})	$U(0, 100)$	0.073 ± 0.005^a	3.06 ± 0.42
a (AU)	$1/a$	0.05258 ± 0.0006	4.19 ± 0.07
$\sqrt{e} \sin \omega$	$U(-1, 1)$	$0.16^{+0.13}_{-0.16}$	0.492 ± 0.044
$\sqrt{e} \cos \omega$	$U(-1, 1)$	$0.36^{+0.10}_{-0.15}$	-0.563 ± 0.039
Mean longitude at 2010.0 λ_{ref} ($^{\circ}$)	$U(-180, 180)$	79.4 ± 4.4	327.2 ± 3.5
Period P(days)	...	4.89 ± 0.00	$3473.53^{+69.40}_{-62.09}$
argument of periastron ω ($^{\circ}$)	...	34^{+111}_{-21}	138.9 ± 4.1
eccentricity e	...	$0.171^{+0.068}_{-0.075}$	0.560 ± 0.036
inclination i ($^{\circ}$) (mode 1)	$\sin i$...	$33.5^{+6.1}_{-4.4}$
Ascending node Ω ($^{\circ}$) (mode 1)	$U(-180, 180)$...	117.1 ± 7.9
inclination i ($^{\circ}$) (mode 2)	$\sin i$...	$143.6^{+4.7}_{-6.2}$
Ascending node Ω ($^{\circ}$) (mode 2)	$U(-180, 180)$...	40 ± 10
orvara Reference Epoch (t_{ref})	2455197.50 BJD

^aan $M_b \sin(i)$ constrain

NOTE—Orbital elements all refer to orbit of the companion about the barycenter. The orbital parameters for the primary about each companion are identical except $\omega_A = \omega + \pi$. We use $\pm\sigma$ to denote the 1σ Gaussian error about the median when the posteriors are approximately symmetric. Otherwise, we denote the value by median $^{+u}_{-l}$ where u and l denote the 68.3% confidence interval about the median. The reference epoch t_{ref} is not a fitted parameter and has no significance within the fit itself, it is the epoch at which the Mean Longitude (λ_{ref}) is evaluated. Mode 1 refers to the orbital parameters derived if one selects the inclination mode with $i < 90$, and mode 2 the converse. The two i/Ω modes yield orbits with otherwise identical parameters (masses, semi-major axis, etc.); visually the orbits are mirror images of each other in 3D space.

cos and Gaia provide only two effective proper motion measurements (with the Hipparcos proper motion being too imprecise to matter). Two proper motions plus an RV curve are insufficient to distinguish prograde from retrograde orbits (Kervella et al. 2020).

The dynamical mass, semi-major axis, and eccentricity of planet c are not significantly affected by the inclination degeneracy. The obliquity between the star A and planet c (ψ_{Ac}), however, is affected. We therefore treat the two modes separately in the following obliquity calculation. We present the posterior probability distribution of obliquity between the star A and planet c as well as between planet b and planet c in the following sections.

4.2. Obliquity between star A and planet c

We separately calculate the obliquity between star A and planet c (ψ_{Ac}) for two scenarios according to possible stellar spin from Sanchis-Ojeda & Winn (2011): star pole-on ($i_{\text{star}} = 168^{\circ} \pm 2^{\circ}$) and star edge-on ($i_{\text{star}} =$

$80^{\circ} \pm 3^{\circ}$). In each scenario, ψ_{Ac} is then calculated separately for two orbital modes: retrograde mode ($i_c > 90^{\circ}$) and prograde mode ($i_c < 90^{\circ}$). The obliquity posterior between star A and the outer planet c is plotted in Figure 5 for the four possible orbital/stellar spin configurations. The upper and bottom panels show the probability density of ψ_{Ac} for star pole-on and edge-on scenarios. These probability densities would not be flat in the absence of constraining data, as two randomly oriented vectors will tend to be closer to perpendicular than to being parallel. This imposes a geometric $\sin \psi$ prior, which we plot as a dashed-violet line for comparison. Deviations from this $\sin \psi$ prior reflect the constraining power of our measurement.

Our posterior on the obliquity between the star and planet c strongly disfavors alignment. Figure 6 shows a zoom-in of the ψ_{Ac} posterior in Figure 5 for the case where the star appears edge-on. Obliquities less than 30° can be ruled out with 99.73% confidence, and obliq-

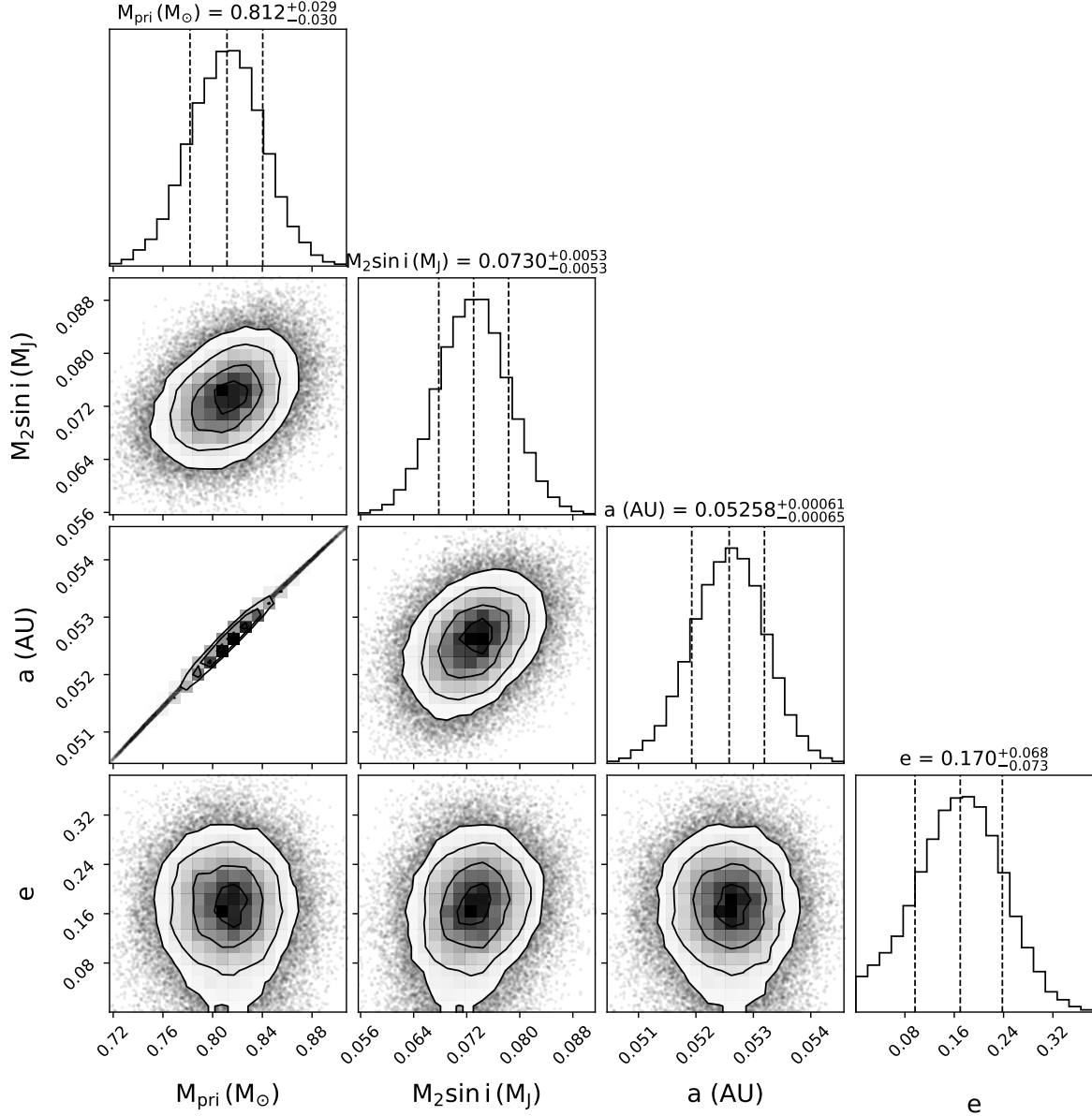


Figure 3. Corner plot of the orbital elements, with respect to the star, for HAT-P-11 b, which demonstrating a constraint on $M_b \sin i$. In the 1D histograms, the vertical-dashed lines about the center dashed lines give the 16% and 84% quantiles around the median. In the 2d histograms, the contours give the 1- σ , 2- σ , and 3- σ levels. The summary statistics of HAT-P-11 system orbit fit are given separately for both inclination modes in Table 1.

uties less than 15 degrees are disfavored by odds of least 15,000-to-1 (i.e., 4 σ confidence).

In all the cases, but especially if HAT-P-11 A is seen edge-on, ψ_{Ac} near 0° are disfavored significantly more than from the $\sin i$ prior alone. In the star pole-on scenario, $\psi_{Ac} > 90^\circ$ and $\psi_{Ac} < 90^\circ$ is strongly ruled out for $i_c > 90^\circ$ and $i_c < 90^\circ$, respectively. The peak value of ψ_{Ac} is around 45° for retrograde mode and around 135° for prograde mode. In the star edge-on scenario, $\psi_{Ac} < 30^\circ$ and $\psi_{Ac} > 150^\circ$ are strongly ruled out for both inclination modes. The maximum value

of ψ_{Ac} is around 70° and the second maximum value is around 135° for retrograde mode. The maximum is around 110° and the second maximum is around 55° for prograde mode. These local maxima extend less than a factor of 2 above the continuum of the probability distribution. While we can determine that planet c's orbit is misaligned with respect to the stellar spin we obtain only a broad constraint on the angle of the misalignment.

4.3. Obliquity between planets b and c

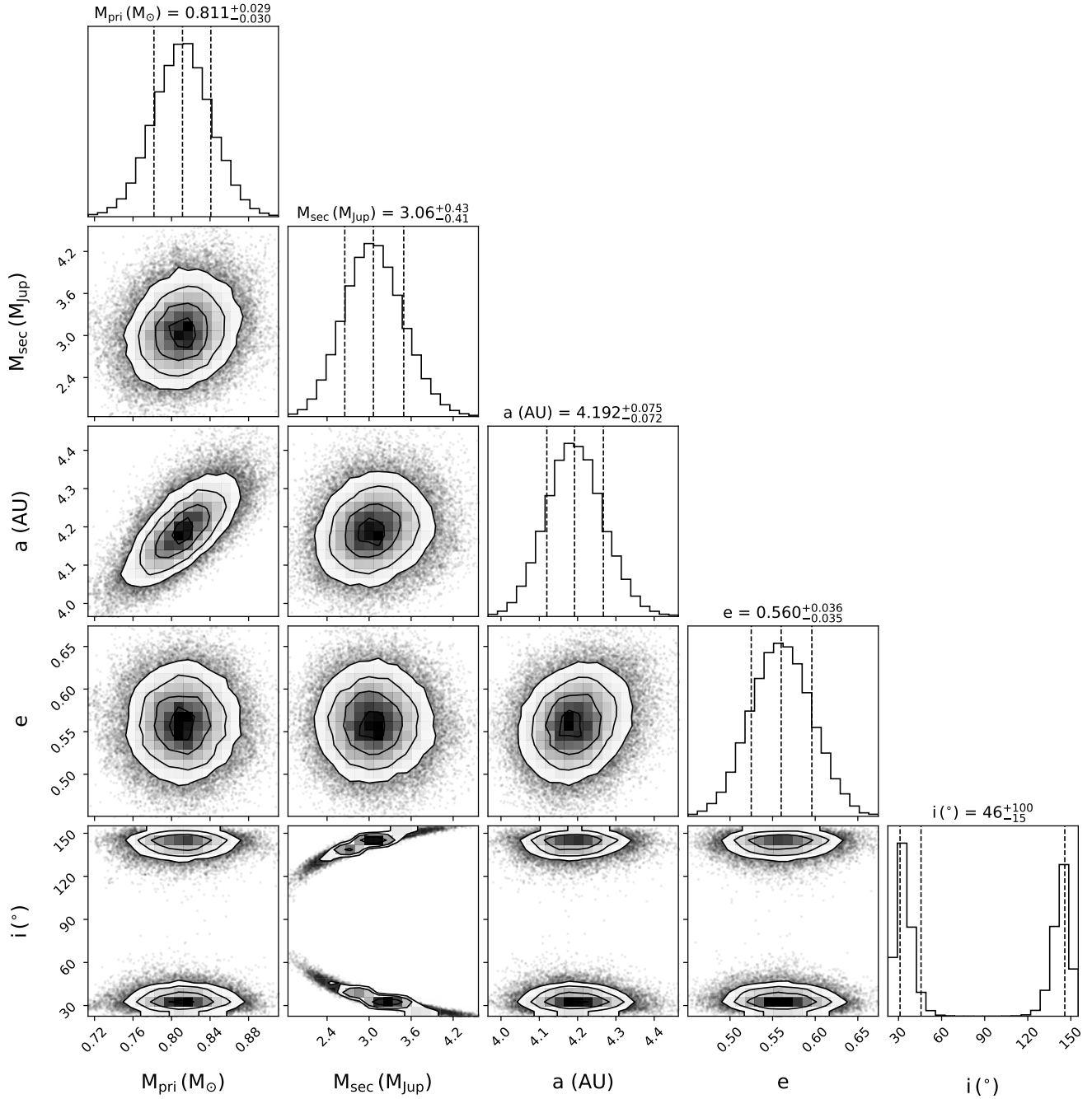


Figure 4. Corner plot of the orbital elements, with respect to the star, for HAT-P-11 c. In the 1D histograms, the vertical-dashed lines about the center dashed lines give the 16% and 84% quantiles around the median. In the 2d histograms, the contours give the 1- σ , 2- σ , and 3- σ levels. The result of inclination is bimodal (shown in lower right 1D histogram), where the peaks of distribution are close to 30° and 150° (two modes are reflected with respect to 90°). The summary statistics of HAT-P-11 system orbit fit are given separately for both inclination modes in Table 1.

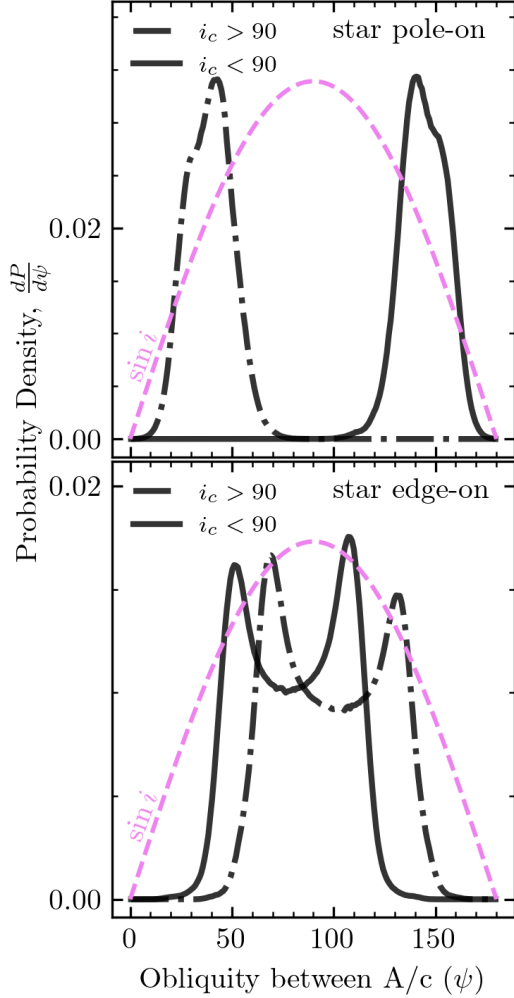


Figure 5. The obliquity posterior between the outer planet HAT-P-11 c and the star A, for the four possible orbital/stellar spin configurations. The top panel shows the two obliquity posteriors (one for each of the possible inclination modes of the planet) assuming the pole-on stellar inclination posterior from [Sanchis-Ojeda & Winn \(2011\)](#). The bottom panel uses the the edge-on stellar inclination posterior. In dashed violet is the geometric $\sin i$ posterior, which would be expected if we had no constraint on the orbit of HAT-P-11 c.

The obliquity between the inner planet b and the outer planet c (ψ_{bc}) is also calculated separately for the two i_c modes. Due to its close-in orbit and extremely short period, we are not able to constrain planet b’s orbital inclination with a combination of absolute astrometry and RV data. Instead, we use the well-determined inclination of $i_b = 88.5^\circ \pm 0.6$ for inner planet b derived from the transit light curve and reported by [Stassun et al. \(2017\)](#).

Figure 7 presents the obliquity posterior between the outer planet c and the inner planet b. In both i_c modes $\psi_{bc} < 30^\circ$ and $\psi_{bc} > 150^\circ$ are strongly ruled out from

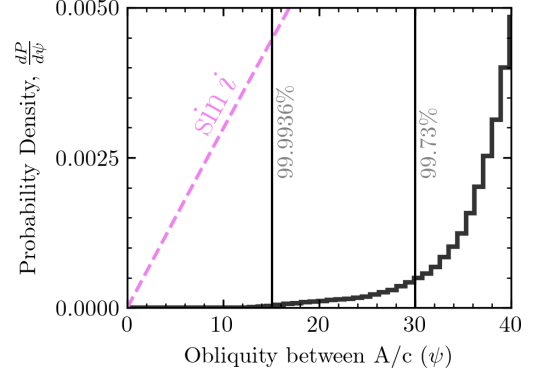


Figure 6. Zoom in of Figure 5 between 0 and 40 degree obliquities. We show the most likely case (edge-on) and the $i_c < 90$ degrees orbital solution. Two lower limits are presented as black vertical lines: the 3σ lower-limit on the obliquity is 30 degrees, and the 4σ (99.9936%) lower-limit is 15 degrees.

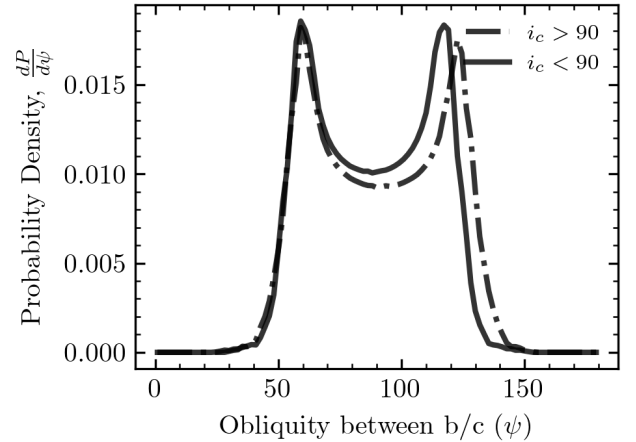


Figure 7. The obliquity posterior between the outer c and the inner planet b, for the two possible i_c configurations, assuming $i_b = 88.5^\circ \pm 0.6$ from [\(Stassun et al. 2017\)](#).

posterior distribution. The peak value of ψ_{bc} is around 60° is presented in both inclination modes, and the other peak resides around 120° for prograde mode and 125° for retrograde mode. The distribution of ψ_{bc} is slightly broader for the retrograde mode than for the prograde mode. Our result of ψ_{bc} makes an improvement over the result of [Xuan & Wyatt \(2020\)](#), with much stronger evidence for misalignment (c.f. the right panel of their Figure 2).

4.4. Gaia Acceleration

The bimodal inclination distribution suggests that, based on the existing data, it is impossible to distinguish whether the planet’s orbit is prograde or retrograde. Future astrometric data from *Gaia* would help break this degeneracy.

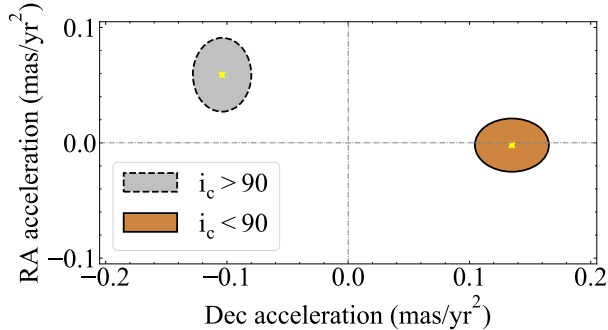


Figure 8. The predicted accelerations for two inclination modes of planet *c*, in unit of milli-arcsecond per year squared. The 1σ contour of the retrograde mode is plotted with a dashed line, and the corresponding contour of prograde mode is shown with a solid line. The center blue crosses indicate the mean values. Zero accelerations in both RA and Dec are marked for reference.

To measure the impact of Gaia on our knowledge of planet *c*'s orbit, we predict what Gaia DR4 could report for the acceleration terms on RA (α) and Dec (δ) using *htof* (Brandt et al. 2021c) and the *Gaia* GOST scanning predictions. We treat the two inclination modes of planet *c* individually for acceleration calculations. These calculations simulate absolute astrometry based on an orbital configuration from our joint posteriors, and then use a seven-parameter fit (linear motion plus constant acceleration) to obtain a Gaia prediction.

Figure 8 plots the acceleration posteriors for both inclination modes of planet *c*'s orbit. A blue cross is plotted at each ellipse indicates the mean value of acceleration, where the area of each ellipse include the 1σ uncertainty in the prediction. These modes will be readily distinguishable by Gaia assuming an acceleration precision better than $\approx 0.1 \text{ mas yr}^{-2}$. Most acceleration measurements in Gaia DR3 already exceed this precision (Halbwachs et al. 2023), while sensitivity to acceleration is a steep function of mission duration thanks to the quadratic dependence of the accumulated signal on time. It appears likely that the next Gaia data release will settle the 3D orientation of planet *c*'s orbit.

5. DISCUSSION AND CONCLUSIONS

Through a combination of absolute astrometry, radial velocity, and transit-derived measurements, we confirm that the three main angular momentum vectors in the HAT-P-11 system are all significantly misaligned. Our constraints on the degree of the misalignment depend on the obliquity between the star and the inner planet, which Sanchis-Ojeda & Winn (2011) determined to be consistent with either a nearly pole-on or a nearly edge-on orientation for the star.

Table 2. Confidence interval of derived obliquities with combined i_c modes, assuming the star to rotate edge-on as seen from Earth.

Parameter	99% confidence	95% confidence
ψ_{Ac}	36°.2 to 147°.3	42°.9 to 137°.9
ψ_{bc}	42°.0 to 134°.0	49°.8 to 130°.0

The case where the star is viewed edge-on produces a greater misalignment (a minimum misalignment of 15° versus a minimum of $\approx 5^\circ$ at 4σ significance), however edge-on is also a more likely scenario for the star. It is geometrically favored, as visualized in Figure 1, by comparing the solid-angle captured by the upper, edge-on cone to the much smaller solid-angle subtended by the lower pole-on cone. Secondly, the edge-on solution produces a rotational velocity more favored by modern measurements. Sanchis-Ojeda & Winn (2011) stated that the pole-on solution predicted a $v \sin i$ for the star of 0.5 km/s, while edge-on was consistent with 1.3 km/s. At the time, both were consistent with the $v \sin i$ measurements available, but as of this publication that is no longer the case. Brewer & Fischer (2018) and Pefigura et al. (2017) measured $v \sin i = 2 \pm 0.5 \text{ km/s}$ and $3.2 \pm 1 \text{ km/s}$, respectively, favoring the edge-on scenario. The edge-on spin case is thus favored by about 2σ to 3σ considering the relative disagreement with $v \sin i$ measurements; and favored by a factor of about 30 geometrically.

Table 2 presents the 99% and 95% confidence intervals of both obliquity posteriors from this work, combining the two inclination modes for planet *c* (i_c), assuming the star to rotate edge-on as seen from Earth. At 2σ significance, the three angular momentum vectors are all misaligned to at least $\approx 40^\circ$, while at 3σ significance, they are all misaligned to at least $\approx 30^\circ$. A companion paper, Paper 2, explores the dynamical origin and history of the HAT-P-11 system.

This work, by using the improvements of Gaia EDR3 (Gaia Collaboration et al. 2020; Lindegren et al. 2020), has significantly improved our knowledge of the three-dimensional structure of the HAT-P-11 system. We present the first constraints on the obliquity between the star and the outer planet, planet *c* ψ_{Ac} , and present an improved ψ_{bc} posterior, indicating a high mutual inclinations within HAT-P-11 system and suggesting a complex dynamical history. Based on the results of this study, Paper 2 explores the origin and evolution of the HAT-P-11 system through a combination of scattering and subsequent tides and migration.

ACKNOWLEDGMENTS

This work makes use of data from Hipparcos-Gaia Catalog of Accelerations (HGCA, Brandt 2018), the High-Resolution Échelle Spectrometer (HIRES, Vogt et al. 1994) on the Keck telescope, the long-running California Planet Search (CPS, Howard et al. 2010), and the RVs tabulated by (Yee et al. 2018).

This work uses `astropy` (Astropy Collaboration et al. 2013; Price-Whelan et al. 2018), `scipy` (Virtanen et al.

2020), `numpy` (Oliphant 2006; van der Walt et al. 2011), `htof` (Brandt & Michalik 2020; Brandt et al. 2021b), `orvara` (Brandt et al. 2021d), and `Jupyter` (<https://jupyter.org/>).

REFERENCES

- Agol, E., Steffen, J., Sari, R., & Clarkson, W. 2005, *MNRAS*, 359, 567, doi: [10.1111/j.1365-2966.2005.08922.x](https://doi.org/10.1111/j.1365-2966.2005.08922.x)
- Agol, E., Dorn, C., Grimm, S. L., et al. 2021, *PSJ*, 2, 1, doi: [10.3847/PSJ/abd022](https://doi.org/10.3847/PSJ/abd022)
- Albrecht, S., Winn, J. N., Marcy, G. W., et al. 2013, *The Astrophysical Journal*, 771, 11
- Astropy Collaboration, Robitaille, T. P., Tollerud, E. J., et al. 2013, *A&A*, 558, A33, doi: [10.1051/0004-6361/201322068](https://doi.org/10.1051/0004-6361/201322068)
- Bakos, G. Á., Torres, G., Pál, A., et al. 2010, *ApJ*, 710, 1724, doi: [10.1088/0004-637X/710/2/1724](https://doi.org/10.1088/0004-637X/710/2/1724)
- Brandt, G. M., Brandt, T. D., Dupuy, T. J., Li, Y., & Michalik, D. 2021a, *AJ*, 161, 179, doi: [10.3847/1538-3881/abdc2e](https://doi.org/10.3847/1538-3881/abdc2e)
- Brandt, G. M., & Michalik, D. 2020, *Zenodo*, doi: [10.5281/zenodo.4118572](https://doi.org/10.5281/zenodo.4118572)
- Brandt, G. M., Michalik, D., & Brandt, T. D. 2023, *RAS Techniques and Instruments*, 2, 218, doi: [10.1093/rasti/rzad011](https://doi.org/10.1093/rasti/rzad011)
- Brandt, G. M., Michalik, D., Brandt, T. D., et al. 2021b, *AJ*, 162, 230, doi: [10.3847/1538-3881/ac12d0](https://doi.org/10.3847/1538-3881/ac12d0)
- . 2021c, *AJ*, 162, 230, doi: [10.3847/1538-3881/ac12d0](https://doi.org/10.3847/1538-3881/ac12d0)
- Brandt, T. D. 2018, *The Astrophysical Journal Supplement Series*, 239, 31, doi: [10.3847/1538-4365/aaec06](https://doi.org/10.3847/1538-4365/aaec06)
- . 2021, *arXiv e-prints*, arXiv:2105.11662, <https://arxiv.org/abs/2105.11662>
- Brandt, T. D., Dupuy, T. J., Li, Y., et al. 2021d, *AJ*, 162, 186, doi: [10.3847/1538-3881/ac042e](https://doi.org/10.3847/1538-3881/ac042e)
- Brewer, J. M., & Fischer, D. A. 2018, *ApJS*, 237, 38, doi: [10.3847/1538-4365/aad501](https://doi.org/10.3847/1538-4365/aad501)
- Chatterjee, S., Ford, E. B., Matsumura, S., & Rasio, F. A. 2008, *The Astrophysical Journal*, 686, 580
- Dai, F., Winn, J. N., Berta-Thompson, Z., Sanchis-Ojeda, R., & Albrecht, S. 2018, *AJ*, 155, 177, doi: [10.3847/1538-3881/aab618](https://doi.org/10.3847/1538-3881/aab618)
- Dawson, R. I. 2014, *ApJL*, 790, L31, doi: [10.1088/2041-8205/790/2/L31](https://doi.org/10.1088/2041-8205/790/2/L31)
- ESA, ed. 1997, *The HIPPARCOS and TYCHO catalogues. Astrometric and photometric star catalogues derived from the ESA HIPPARCOS Space Astrometry Mission*, ESA Special Publication
- Foreman-Mackey, D., Hogg, D. W., Lang, D., & Goodman, J. 2013, *PASP*, 125, 306, doi: [10.1086/670067](https://doi.org/10.1086/670067)
- Gaia Collaboration, Brown, A. G. A., Vallenari, A., et al. 2020, *arXiv e-prints*, arXiv:2012.01533, <https://arxiv.org/abs/2012.01533>
- Gaia Collaboration, Prusti, T., de Bruijne, J. H. J., et al. 2016, *A&A*, 595, A1, doi: [10.1051/0004-6361/201629272](https://doi.org/10.1051/0004-6361/201629272)
- Gillon, M., Triaud, A. H., Demory, B.-O., et al. 2017, *Nature*, 542, 456
- Halbwachs, J.-L., Pourbaix, D., Arenou, F., et al. 2023, *A&A*, 674, A9, doi: [10.1051/0004-6361/202243969](https://doi.org/10.1051/0004-6361/202243969)
- Hirano, T., Narita, N., Shporer, A., et al. 2011, *PASJ*, 63, 531, doi: [10.1093/pasj/63.sp2.S531](https://doi.org/10.1093/pasj/63.sp2.S531)
- Holman, M. J., & Murray, N. W. 2005, *Science*, 307, 1288, doi: [10.1126/science.1107822](https://doi.org/10.1126/science.1107822)
- Howard, A. W., Johnson, J. A., Marcy, G. W., et al. 2010, *ApJ*, 721, 1467, doi: [10.1088/0004-637X/721/2/1467](https://doi.org/10.1088/0004-637X/721/2/1467)
- Kane, S. R., & Torres, S. M. 2017, *AJ*, 154, 204, doi: [10.3847/1538-3881/aa8fce](https://doi.org/10.3847/1538-3881/aa8fce)
- Kervella, P., Arenou, F., & Schneider, J. 2020, *A&A*, 635, L14, doi: [10.1051/0004-6361/202037551](https://doi.org/10.1051/0004-6361/202037551)
- Kozai, Y. 1962, *AJ*, 67, 591, doi: [10.1086/108790](https://doi.org/10.1086/108790)
- Li, G., & Winn, J. N. 2016, *ApJ*, 818, 5, doi: [10.3847/0004-637X/818/1/5](https://doi.org/10.3847/0004-637X/818/1/5)
- Li, Y., Brandt, T. D., Brandt, G. M., et al. 2021, *AJ*, 162, 266, doi: [10.3847/1538-3881/ac27ab](https://doi.org/10.3847/1538-3881/ac27ab)
- Lidov, M. L. 1962, *Planet. Space Sci.*, 9, 719, doi: [10.1016/0032-0633\(62\)90129-0](https://doi.org/10.1016/0032-0633(62)90129-0)
- Lindgren, L., Klioner, S. A., Hernández, J., et al. 2020, *arXiv e-prints*, arXiv:2012.03380, <https://arxiv.org/abs/2012.03380>
- McLaughlin, D. B. 1924, *ApJ*, 60, 22, doi: [10.1086/142826](https://doi.org/10.1086/142826)
- Morton, T. D., & Winn, J. N. 2014, *ApJ*, 796, 47, doi: [10.1088/0004-637X/796/1/47](https://doi.org/10.1088/0004-637X/796/1/47)

- Nagasawa, M., & Ida, S. 2011, *The Astrophysical Journal*, 742, 72
- Nesvorný, D. 2018, *ARA&A*, 56, 137, doi: [10.1146/annurev-astro-081817-052028](https://doi.org/10.1146/annurev-astro-081817-052028)
- Oliphant, T. 2006, *NumPy: A guide to NumPy, USA*: Trelgol Publishing. <http://www.numpy.org/>
- Petigura, E. A., Howard, A. W., Marcy, G. W., et al. 2017, *AJ*, 154, 107, doi: [10.3847/1538-3881/aa80de](https://doi.org/10.3847/1538-3881/aa80de)
- Price-Whelan, A. M., Sipőcz, B. M., Günther, H. M., et al. 2018, *AJ*, 156, 123, doi: [10.3847/1538-3881/aabc4f](https://doi.org/10.3847/1538-3881/aabc4f)
- Rossiter, R. A. 1924, *ApJ*, 60, 15, doi: [10.1086/142825](https://doi.org/10.1086/142825)
- Sanchis-Ojeda, R., & Winn, J. N. 2011, *ApJ*, 743, 61, doi: [10.1088/0004-637X/743/1/61](https://doi.org/10.1088/0004-637X/743/1/61)
- Souami, D., & Souchay, J. 2012, *Astronomy & Astrophysics*, 543, A133
- Stassun, K. G., Collins, K. A., & Gaudi, B. S. 2017, *AJ*, 153, 136, doi: [10.3847/1538-3881/aa5df3](https://doi.org/10.3847/1538-3881/aa5df3)
- Valsecchi, F., & Rasio, F. A. 2014, *ApJ*, 786, 102, doi: [10.1088/0004-637X/786/2/102](https://doi.org/10.1088/0004-637X/786/2/102)
- van der Walt, S., Colbert, S. C., & Varoquaux, G. 2011, *Computing in Science and Engineering*, 13, 22, doi: [10.1109/MCSE.2011.37](https://doi.org/10.1109/MCSE.2011.37)
- van Leeuwen, F. 2007, *A&A*, 474, 653, doi: [10.1051/0004-6361:20078357](https://doi.org/10.1051/0004-6361:20078357)
- Virtanen, P., Gommers, R., Oliphant, T. E., et al. 2020, *Nature Methods*, 17, 261, doi: <https://doi.org/10.1038/s41592-019-0686-2>
- Vogt, S. S., Allen, S. L., Bigelow, B. C., et al. 1994, in *Proc. SPIE*, Vol. 2198, *Instrumentation in Astronomy VIII*, ed. D. L. Crawford & E. R. Craine, 362, doi: [10.1117/12.176725](https://doi.org/10.1117/12.176725)
- von Zeipel, H. 1910, *Astronomische Nachrichten*, 183, 345, doi: [10.1002/asna.19091832202](https://doi.org/10.1002/asna.19091832202)
- Vousden, W. D., Farr, W. M., & Mandel, I. 2016, *MNRAS*, 455, 1919, doi: [10.1093/mnras/stv2422](https://doi.org/10.1093/mnras/stv2422)
- Winn, J. N., Johnson, J. A., Howard, A. W., et al. 2010, *ApJL*, 723, L223, doi: [10.1088/2041-8205/723/2/L223](https://doi.org/10.1088/2041-8205/723/2/L223)
- Xuan, J. W., & Wyatt, M. C. 2020, *MNRAS*, 497, 2096, doi: [10.1093/mnras/staa2033](https://doi.org/10.1093/mnras/staa2033)
- Yee, S. W., Petigura, E. A., Fulton, B. J., et al. 2018, *AJ*, 155, 255, doi: [10.3847/1538-3881/aabfec](https://doi.org/10.3847/1538-3881/aabfec)
- Zanazzi, J. J., & Lai, D. 2018, *MNRAS*, 478, 835, doi: [10.1093/mnras/sty1075](https://doi.org/10.1093/mnras/sty1075)